SANDIA REPORT

SAND2013-4274
Unlimited Release
Printed May 2013

WO$_3$/TiO$_2$ Nanotube Photoanodes for Solar Water Splitting with Simultaneous Wastewater Treatment

Karla R. Reyes, and David B. Robinson

Sandia National Laboratories

WO$_3$/TiO$_2$ Nanotube Photoanodes for Solar Water Splitting with Simultaneous Wastewater Treatment

Karla R. Reyes*, and David B. Robinson[†]
Materials Chemistry (8223)* and Energy Nanomaterials (8651)[†]
Sandia National Laboratories
P.O. Box 969
Livermore, California 94551-MS9403

Abstract

Nanostructured WO$_3$/TiO$_2$ nanotubes with properties that enhance solar photoconversion reactions were developed, characterized and tested. The TiO$_2$ nanotubes were prepared by anodization of Ti foil, and WO$_3$ was electrodeposited on top of the nanotubes. SEM images show that these materials have the same ordered structure as TiO$_2$ nanotubes, with an external nanostructured WO$_3$ layer. Diffuse reflectance spectra showed an increase in the visible absorption relative to bare TiO$_2$ nanotubes, and in the UV absorption relative to bare WO$_3$ films. Incident simulated solar photon-to-current efficiency increased from 30% (for bare WO$_3$) to 50% (for WO$_3$/TiO$_2$ composites). With the addition of diverse organic pollutants, the photocurrent densities exhibited more than a 5-fold increase. Chemical oxygen demand measurements showed the simultaneous photodegradation of organic pollutants. The results of this work indicate that the unique structure and composition of these composite materials enhance the charge carrier transport and optical properties compared with the parent materials.

Acknowledgments

Contents

Figures

Tables

1. Introduction

Solar energy is potentially clean, safe and limitless, but its use at global scale would benefit from efficient conversion of the energy into a fuel to allow storage and distribution. For solar photoconversion, specialized semiconductors are needed to absorb sunlight and use this energy to drive photochemical reactions. Metal oxides, in particular TiO_2 and WO_3, have properties such as electronic band structure, high photoactivity, chemical stability and low cost that make them good candidates for photoanodic reactions in aqueous electrolytes. However, the efficiency of these materials is still too low for commercial use. There are three factors that are jeopardizing the incident photon-to-current efficiency (IPCE) of metal oxides: (1) poor absorption of solar light, (2), poor charge-carrier transport within the metal oxide, and (3) poor interfacial charge transfer, each represented as an efficiency η in Equation 1.

$$IPCE = \eta_{e^-/h^+} \cdot \eta_{transport} \cdot \eta_{interface} \text{ (Equation 1)}$$

As described below big improvements have been achieved in the efficiency of these processes individually, however the overall efficiency has not been significantly improved. The modifications to improve one process sometimes jeopardizes the other processes. The approach of the present work is to design a solar cell system that corrects each of the limiting factors in a synergistic way (**Table 1**). This system uses nanostructured materials as photoanodes in a photoelectrochemical solar cell, where organic pollutants are photo-degraded (oxidized) on the photoanode, simultaneously producing a high electron flux to the cathode (Figure 1).

Table 1. Proposed solutions to improve the solar cell efficiency.

Problem	Poor transport	Poor absorption	Poor transfer
Process	$\eta_{transport}$	η_{e^-/h^+}	$\eta_{interface}$
Proposed Solution	Organized nanostructures (TiO_2 nanotubes)	Composite materials (WO_3/TiO_2) with long absorption pathway	Add organic pollutants with a fast oxidation rate
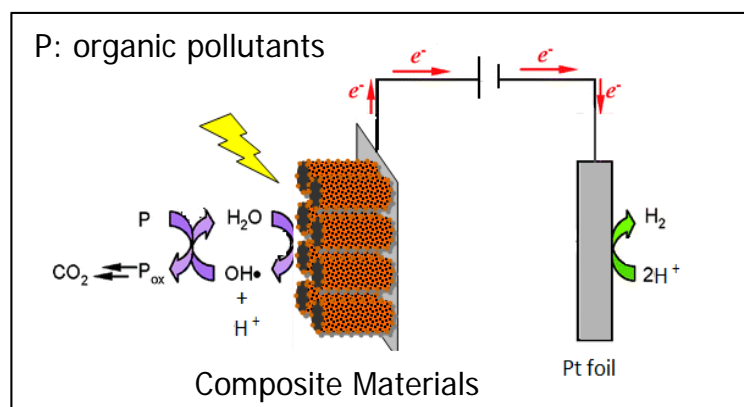
Figure 1. Diagram of the combined waste treatment and energy harvesting photo-electrochemical device.

One of the most studied approaches to increase the visible absorption of metal oxides is compositional doping with anions or transition metals. Due to its electronic bandgap (E_g = 3.2 eV, corresponding to a light wavelength λ = 380 nm), TiO_2 absorbs less than 5 % of the natural solar spectrum. Nitrogen doping has been successfully used to increase the visible absorption of TiO_2, however the efficiency is even worse because N dopants can change the host material crystal structure and act as recombination centers[1]. Other approach to shift the absorption edge toward visible light region is coupling TiO_2 with another metal oxide with narrower bandgap, such as WO_3 (E_g = 2.6 eV, λ = 477 nm). Contrary to other bandgap narrowing approaches (e.g. doping), the coupling approach is expected to provide a better charge separation, which could also increase the charge transport efficiency [2].

After the photons are absorbed and electron-hole pairs e-/h+ are created, the next process transport each of the carriers to other phases or regions before recombination occurs. Control over the morphology of absorber materials, to facilitate orthogonalization of charge separation and charge transport, is attracting significant attention for application in solar energy-conversion devices.[3-11] The one-dimensional morphology allows for electrons move axially along the length of the nanotubes providing direct and faster electron transport to the back to the contact, while photogenerated holes are separated and collected over relatively short distances in an orthogonal direction (Figure 2). In addition, the nanotube architecture has a large internal surface area and can be easily filled with liquid thus enabling intimate contact with electrolyte [1].
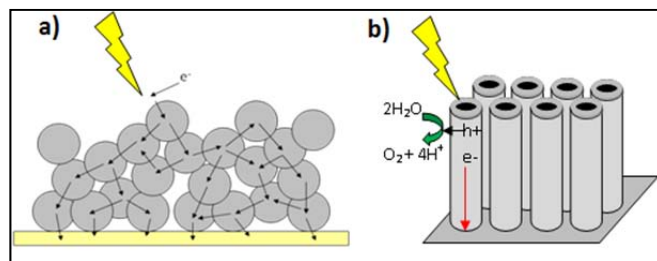
Figure 2. Comparison of the electron pathway in (a) nanoparticles and (b) nanotubes.

Several studies demonstrated that the organized nanostructures enhanced the internal quantum yields and the effective minority-carrier diffusion lengths, consequently reducing the electron-hole recombination of metal oxides [1]. However, the photocurrents of nanostructures are limited by low light absorption and the IPCE values are not significantly improved. Methods of obtaining nearly complete light absorption can be expected to produce very high external quantum yield values for use in optimized solar energy conversion devices. Increasing the optical absorption of films has been a challenge for a number of nanostructured materials, including WO_3 [12-14]. In contrast, TiO_2 nanotubes have been grown as long as several hundreds of microns by anodization [15, 16]. A key drawback of WO_3 is that up to now no highly defined tubular structures could be grown, and thus the full potential of WO_3 based nanotubular systems could not be exploited [12]. In this work, we investigated the use of TiO_2 nanotubes as skeleton to develop WO_3 nanostructures with long absorption pathways.

When the photo-generated charges reach the electrode/electrolyte interface, they have to be used quickly. Due to rapid recombination of the photo-generated electrons and holes and the slow oxidation of water, it is difficult to achieve stoichiometric water splitting. Sacrificial reagents

have been used to react irreversibly with the photo-generated holes resulting in higher quantum efficiency. The remaining strongly reducing electrons can reduce protons to hydrogen molecules in a process known as nonstoichiometric water splitting. Many organic pollutants in wastewater are good electron donors and can be used as the donors for photocatalytic hydrogen evolution [17].

In this work, we developed a low-cost synthetic approach to prepare nanostructured WO_3/TiO_2 composite nanotube substrates. The morphology, crystal structure and optical properties of these new materials were analyzed. Diffuse reflectance spectra of composite WO_3/TiO_2 show an improvement in the visible absorption relative to bare TiO_2 nanotubes and in the UV absorption relative to bare WO_3 films. Photo-electrochemical studies were conducted by employing these materials as photoanodes. Incident photon-to-current efficiency (IPCE) increased from 30% (for bare WO_3) to 50% (for WO_3/TiO_2 composites) and extended up to the visible region (575 nm). The photocurrent density in the presence of common organic pollutants exhibited more than a 5-fold increase. Chemical oxygen demand (COD) measurements demonstrated a simultaneous photo-degradation of those pollutants, reaching 40% removal efficiency after 5h of illumination.

2. Materials and procedures

2.1   Preparation of WO$_3$/TiO$_2$ photoanodes

The fabrication of the WO$_3$/TiO$_2$ materials presented here involved two processes. The first process is the preparation of TiO$_2$ nanotubes by anodization. Ti foil (0.25 mm and 99.7% trace metal basis, Aldrich) was cleaned with acetone, deionized water and methanol and dried under a stream of N$_2$ gas. Ti foil was cut in pieces of 2 by 4 cm and used as the anode. The back of the foil was covered with insulating tape. Pt gauze (Aldrich, 100 mesh, 425 mg, 25mm X 25 mm) was used as the cathode. A Teflon beaker was used as electrochemical cell and the electrolyte solution used was NH$_4$F (0.3 wt %) in an ethylene glycol (EG)-water mixture (ratio of 95:5). The reaction was driven by a dc power supply. All the experiments were carried out at room temperature. The TiO$_2$ nanotubes used for the following reactions were prepared by two-step process. In the first step (or pretreatment step), a Ti foil was anodized at 50 V overnight (around 15 h). Then, the nanotube layer was removed ultrasonically in deionized waster and the remaining foil was dried under a stream of N$_2$ gas.   In the second step, the pretreated foil was anodized again at 50 V during various time periods between 1 and 5 h. The TiO$_2$ nanotubes were annealed in air at 500° C for 2 h.

The second process is the electrodeposition of WO$_3$ on the TiO$_2$ nanotubes. The deposition solution was prepared by dissolving Na$_2$WO$_4$ salt (Aldrich) in deionized water and adding concentrated hydrogen peroxide (30%), which can bind to the anion and improve its solubility at low pH. The salt concentration was 25 mM and hydrogen peroxide concentration was 30 mM. The pH of the resulting solution was 10.4 ± 0.1. Nitric acid was added subsequently in order to adjust the pH down to 1.4. The solution was prepared the day of the deposition experiments. The electrodeposition experiments were performed in a three-electrode Teflon electrochemical cell at room temperature. The annealed TiO$_2$ nanotubes were used as a substrate. The reference electrode was Ag/AgCl and the counter electrode was a platinum gauze. A SP-200 Potentiostat (Bio-Logic Science Instruments) was used to apply a potential of -0.437 V vs. Ag/AgCl (-0.24 V vs. NHE) and recorded the charge density during the deposition experiments. The resulting composite materials were annealed in air at 400° C for 2 h.

For comparison purposes, TiO$_2$ nanoparticle electrodes were made with commercial TiO$_2$ nanopowder (Degussa P25). 5 g TiO$_2$ P25 were mixed with 0.5 mL acetic acid and 8 mL DI water, in a ceramic mortar using a pestle and ground for 15 min. TiO$_2$ P25 paste was spread on conductive fluorine-doped tin oxide film (FTO) on glass. The film was dried at room temperature for 1 h and then annealed in air at 500° C for 2 h.

2.2   Characterization

The samples on the foil were analyzed by scanning electron microscopy-energy-dispersive X-ray spectroscopy (SEM-EDS) and X-ray diffraction (XRD). Morphological characterization was carried out on a JEOL JSM7600F Thermal Field Emission SEM. Top views of the TiO$_2$

nanotubes were taken before and after WO_3 electroplating. For the cross-sectional views, the foil was bent and the film was broken and detached from the foil. Several areas of the film were analyzed using an EDS (Oxford XMax with 80mm² detector) that was coupled to the SEM. Crystal structures were collected by Empyrean X-ray diffraction spectrometer and data was analyzed by X'Pert High Score Plus software. For the optical properties, the absorption spectra of the films were collected using Shimadzu UV-2101PC spectrometer with a diffuse reflectance adapter.

2.3 Photoelectrochemical and photodegradation analysis

For photoelectrochemical measurements, the back of the foil was gently polished to remove any oxides. Conductive silver epoxy was then used to attach a copper wire to the backside of the foil. The metallic contact and the foil edges were then covered with Hysol 1C epoxy to produce an exposed area of 0.8-1.2 cm^2. The contact wire was threaded through a glass tube, and the electrode was attached to the end of the tube through the use of Hysol 1C epoxy. The electrodes were allowed to cure for > 12 h at 60 ºC. The area of the electrode was measured by taking a digital image, using a flat bed scanner, of the electrode and of a calibration scale. The resulting images were analyzed using ImageJ software.

A Teflon electrochemical cell with a quartz window, a platinum foil counter electrode, and Ag/AgCl reference was used for all photoelectrochemical studies. A solar simulator (ABET Technologies, model 10500) with an Air Mass (AM) = 1.5 filter set was used as an illumination source. The intensity of the Xe lamp was measured using a solar power meter (calibrated with a standard Si photodiode), and the incident illumination intensity was adjusted by changing the position of the lamp relative to that of the electrochemical cell. For all the photoelectrochemical experiments, except for IPCE measurements, an intensity of 100 mW/cm^2 (equivalent to 1 sun) was used to illuminate the cell. No correction was made for optical reflection and scattering losses, but it is expected that some of light intensity is loss when the light goes through the quartz window and the electrolyte before reaching the electrode. The electrolyte was aqueous 0.10 M H_2SO_4 (pH = 1.4) for all experiments, a typical volume used was 40 mL. Electrochemical measurements were recorded using a SP-200 Potentiostat (Bio-Logic Science Instruments). Photocurrent densities were calculated as the difference between currents (corrected for the electrode area) that were recorded in the presence and absence of illumination, acquired consecutively. For measurements under visible light, a cut-on ($\lambda > 400$ nm) filter was used. Methanol, formic acid, formaldehyde and ethylene glycol were used as organic pollutant models and added to the supporting electrolyte in controlled amounts from 0.1 M up to 3 M depending of the compound solubility.

For IPCE measurements, a monochromator was placed in front of the solar simulator. The data was collected every 25 nm from 300 nm to 600 nm. The following equation was used the IPCE values at each measured wavelength.

$$IPCE = \frac{J \times 1239.8}{P \times \lambda} \quad \textbf{(Equation 2)}$$

12

where J is the photocurrent density in mA/cm^2, P is the calibrated monochromated illumination power intensity in mW/cm^2, λ is the wavelength in nm at which this illumination power is measured and 1239.8 in V x nm represents a multiplication of Planck's constant and the speed of light. The peak center and FWHM was determined with a Stellar Net mini-spectrometer. FWHM was between 4.5 to 7.0 nm. The power intensity was determined before and after each experiment with a Gentec-EO power meter (item number 201751) with a chopper and lock in amplifier.

For photodegradation analysis, the dichromate COD high range method and a chemical oxygen demand (COD) photometer (HI 83099 from Hanna Instrument) were used to calculate the COD removal efficiency.

$$Removal\ efficiency = \left(\frac{COD_{initial} - COD}{COD_{initial}}\right) \times 100 \quad \textbf{(Equation 3)}$$

The photocurrent was collected continuously during the whole experiment. A control experiment was performed using the methodology, but with no electrodes, in order to measure the loss of organic pollutants for evaporation. To avoid the evaporation, the quartz beaker was covered with parafilm and the aliquots at different times were collected using a syringe. 0.2 mL of the sample was added to the pre-dosed reagent vial (HI 93754C, Hanna Instrument) and mixed by inverting the vial a couple of times. The vials were heated for 2h at 150 C in the test tube heater (HI 740216) and then analyzed with the photometer (HI 83099).

3. Results and discussion

3.1 Synthesis of Nanostructured WO$_3$ / TiO$_2$ nanotubes

In the last decade, several studies demonstrate that organized nanostructures, such as nanorods, nanotubes and nanowires, improve the charge carrier transport compared to compact electrodes or nanoparticle networks. [18]. However, the low surface packing of one-dimensional nanostructures affects the absorption at the optical plane. Increasing the optical absorption of films has been a challenge for a number of nanostructured materials. In contrast to TiO$_2$ nanotubes [15], achieving thick, well-defined, porous WO$_3$ structures by anodization has been more difficult, due to solubility issues [19]. The formation of micrometer thick porous WO$_3$ films (up to 2 µm) has been recently reported by the anodization of W foil [19]. Optimization studies of anodization parameters indicated that longer anodization times yielded thicker porous layers, but at the same time, the pore diameter increased, reducing the packing fraction. The development of synthetic methods for achieving nearly complete light absorption is thus needed to develop more efficient nanostructured photoelectrodes from this material system.

A strategy explored by Benoit et al. dip coats TiO$_2$ nanotubes (NTs) with a solution of WCl$_6$ to get, after annealing, an inhomogeneous coat of monoclinic WO$_3$ on the surface of the NT array [12]. Lai et al. sputter deposited W onto a TiO$_2$ NT array. At low sputtering power (< 180 W), TiO$_2$ nanotubes preserved the high-ordered structures, however, at higher power (> 180 W) the nanotubes collapsed [20]. Nah et al. showed that composite TiO$_2$-WO$_3$ NTs can be fabricated by anodization of a TiW alloy [13]. Park et al. prepared a WO$_3$ coated TiO$_2$ nanotube array by electrochemical deposition of WO$_3$ sol to TiO$_2$ nanotube array. All these previous attempts produced TiO$_2$ nanotubes decorated with thin WO$_3$ nanoparticle layers, however, WO$_3$ didn't show any organized structure by itself.

The synthetic approach of this work is to increase the absorption pathway of WO$_3$ using TiO$_2$ nanotubes as a support structure (or skeleton).

Figure 3 shows the two-step process synthesis developed to prepare the composite materials. First step, TiO$_2$ nanotubes were prepared by anodization of Ti foil. Therefore, the nanotubes were used a substrate for WO$_3$ electrodeposition in the second step.
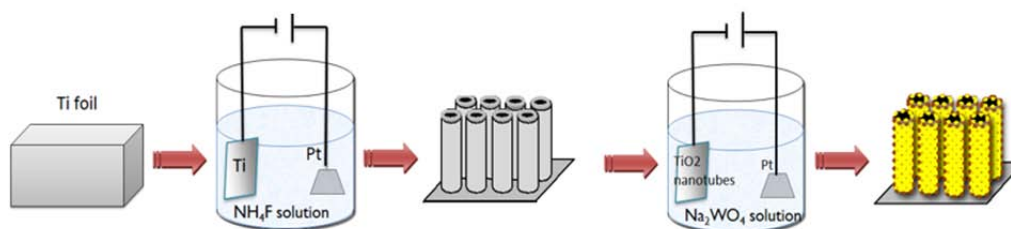
Figure 3. Two-step synthetic approach to prepare WO$_3$/TiO$_2$ nanotubes.

3.1.1 TiO$_2$ nanotube anodization

SEM images (Figure 4) showed that after the first anodization, the TiO$_2$ nanotubes are in a disordered array due to the corrugated surface of the Ti foil. After the nanotube layer was removed ultrasonically, an imprint pattern was left on the foil, which acts as template in the further growth of well-aligned nanotubes. The nanotubes are highly uniform and vertically oriented with an opening (mouth) of 100 nm in diameter and walls with a thickness of around 10 nm. The length of the nanotubes is proportional to the anodization time. For anodization times of 1, 2 and 5h, the length of the nanotubes according SEM cross sectional images was 6, 12 and 20 µm respectively. According to previous studies, TiO$_2$ nanotubes with a length between 15- 20 µm showed the highest photoactivity [1]. For that reason, the composite materials were prepared using TiO$_2$ nanotubes anodized for 5h.

100 nm   1 µm   100 nm
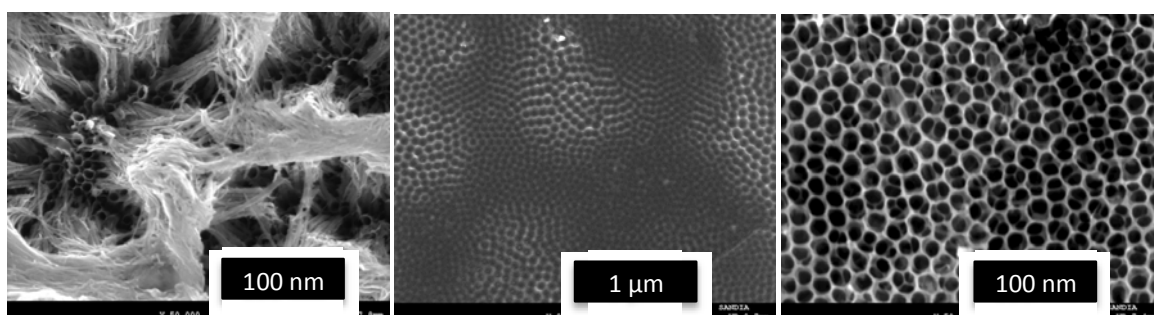
Figure 4. SEM images of TiO$_2$ nanotubes (left) first anodization, (center) Ti foil after nanotube layer removed and (right) second anodization.

3.1.2 WO$_3$ electrodeposition

High quality WO$_3$ films are most generally obtained by vacuum evaporation and sputtering. Unfortunately, these methods are time consuming and expensive. Wet low-cost methods, such as electrodeposition, seem to be very promising approach to create WO$_3$ films. The film electrodeposition method is based on the cathodic reduction of a peroxo precursor, which is obtained by mixing a tungsten precursor with an excess of hydrogen peroxide. The precursor is described as a dimer with the formula $W_2O_{11}^{2-}$ with (O$_2$) a peroxide ligand [21]. The oxidation state of W is +VI. The deposition reaction is described as:

$$W_2O_{11}^{2-} + (2 + x)H^+ + xe^- \rightarrow 2\ WO_3 + (2 + x)/2H_2O + (8 - x)/4O_2$$

It has been shown that parallel parasitic reactions take place and should correspond to hydrogen evolution, colloidal WO$_3$ formation and reduction of free H$_2$O$_2$, residual O$_2$ and polytungstate. Due to all the parasitic reactions and uncertainty of the deposition efficiency and stoichiometry, we report deposited amounts in deposited charge density (mAh) instead of moles.
Annealed TiO$_2$ nanotubes were used as a substrate for WO$_3$ electrodeposition. The annealing of TiO$_2$ is needed before the deposition experiments because amorphous TiO$_2$ partially dissolved in the tungstic acid solution. We observed that WO$_3$ electrodeposition on flat substrates suffers

adhesion problems. The WO_3 control samples prepared on Ti foil or FTO glass were spontaneously separated from the substrate after being tested in the electrochemical cell. However, using nanotubes as a substrate, WO_3 samples showed excellent adhesion and connectivity to the substrate and excellent structural stability. In addition, this synthesis offers an easy control of the morphology through the synthetic parameters. For instance, the length of the TiO_2 nanotubes can be controlled by the anodization time and the WO_3 nanostructures can be modified by the electrodeposition time. This low-cost process can be easily scaled-up to produce larger samples and can be adapted for the preparation of other composite nanostructured materials.

Table 2. WO_3 electrodeposition time, electrode area and charge density of composite WO_3/TiO_2 samples.

Sample label	WO_3 electrodeposition time (min)	area (cm^2)	dQ (mA.h)	charge density $(mA.h/cm^2)$
TiO_2/WO_3 (5 min)	5	2.761	0.360	0.130
TiO_2/WO_3 (10 min)	10	4.216	0.950	0.225
TiO_2/WO_3 (15 min)	15	3.692	1.115	0.302

3.2   Crystal structure and composition

Figure 5 shows the X-ray diffraction (XRD) patterns of WO_3/TiO_2 composite films that had been annealed at 400 °C in air for 2 h, as a function of the WO_3 electrodeposition time. TiO_2 nanotubes show the distinct peaks of the anatase phase. No other XRD peaks except for Ti foil peaks were detected, indicating presence of a single type of crystalline compound. After the WO_3 electrodeposition, the films showed three additional distinct peaks in the range $23º < 2\theta < 25º$ indicate that the samples are composed of TiO_2 and WO_3. The three peaks are more defined as the electrodeposition time increases. WO_3, despite its simple stoichiometry, can be found in large variety of crystal structures (e.g. monoclinic, orthorhombic and triclinic) [22, 23]. Comparing the XRD patterns with the JCPD reference files, the diffraction peaks resemble those of monoclinic structure (JCPD # 43-1035), the most stable phase at room temperature and a photoactive phase of WO_3 [24, 25]. No additional peaks were detected, indicating the absence of crystalline Ti-W alloys.

EDS was performed in at least five different areas in the same sample in order to accurately represent the whole sample. The main elements found in the samples were titanium, oxygen and tungsten (Figure 6). Trace amounts of gold were detected because gold was sputtered on the sample to avoid charging. Table 3 summarizes the atomic percentages (at %) determined by averaging EDS data in several represented zones in the samples. As expected, the W atomic percent increases and the Ti atomic percent decreases as the electrodeposition time increases.
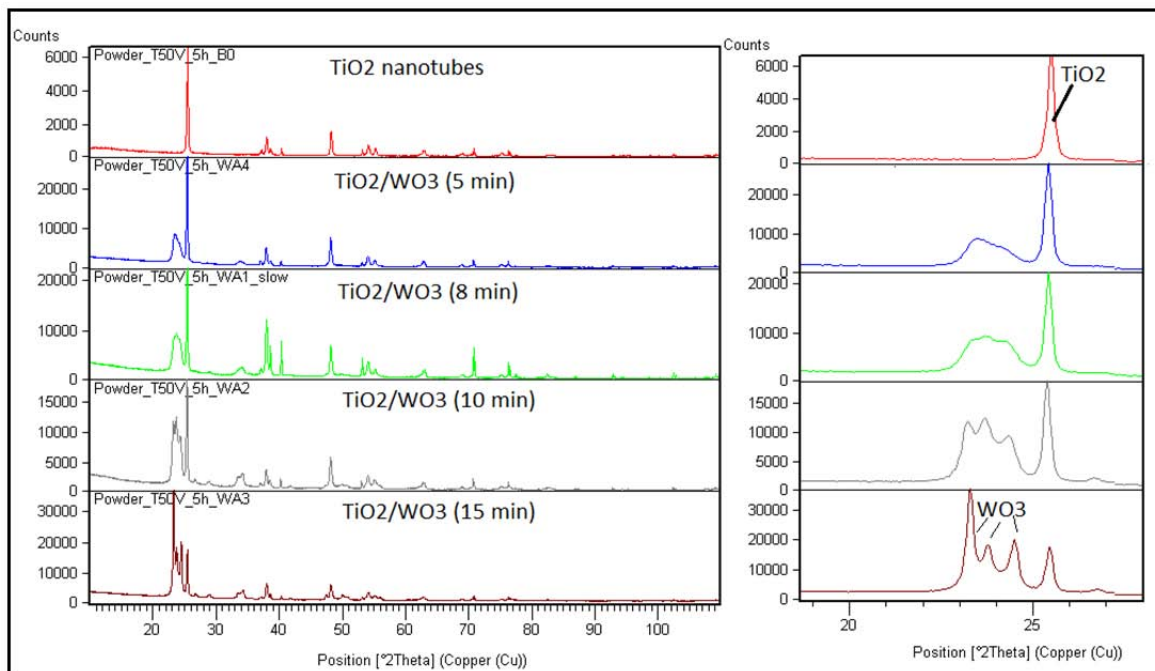
Figure 5. XRD patterns of TiO_2 and WO_3/TiO_2 composite materials

Table 3. Average atomic percentages (at %) of the main elements found in EDS spectra.

Sample	O (at %)	Ti (at %)	W (at %)
TiO_2	72	28	0
TiO_2/WO_3 (5 min)	69	21	10
TiO_2/WO_3 (10 min)	71	15	14
TiO_2/WO_3 (15 min)	73	8	19
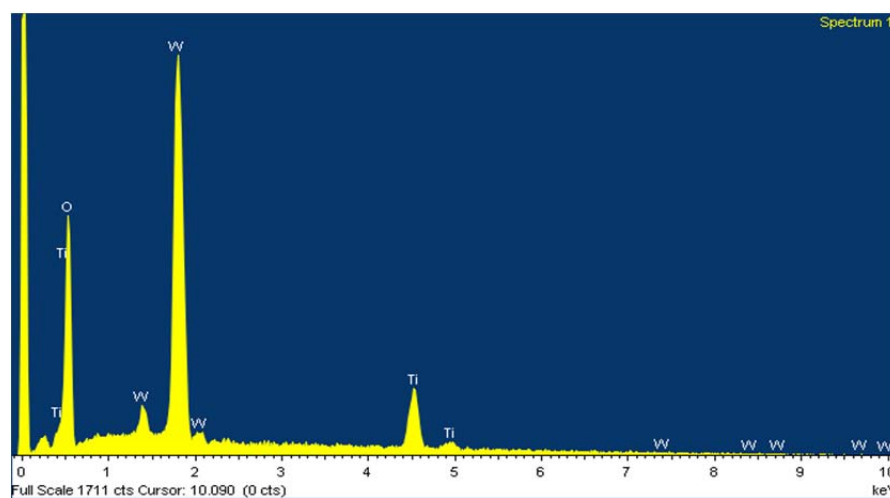
Figure 6. Representative EDS spectrum of WO_3/TiO_2 materials**.**

18

3.3   Optical properties

Figure 7 shows the UV and visible absorption of WO_3/TiO_2 composites, TiO_2 nanotubes only, and WO_3 only. TiO_2 nanotubes showed an almost complete absorption of UV light up to 375 nm. WO_3 nanoparticles absorbed less than half of the incident light up to 480 nm. WO_3/TiO_2 nanotubes absorb almost all the UV light and extend the absorption up to the visible region. Diffuse reflectance spectra showed an improvement in the visible absorption relative to bare TiO_2 nanotubes and more than twice the UV absorption relative to WO_3 nanoparticles.
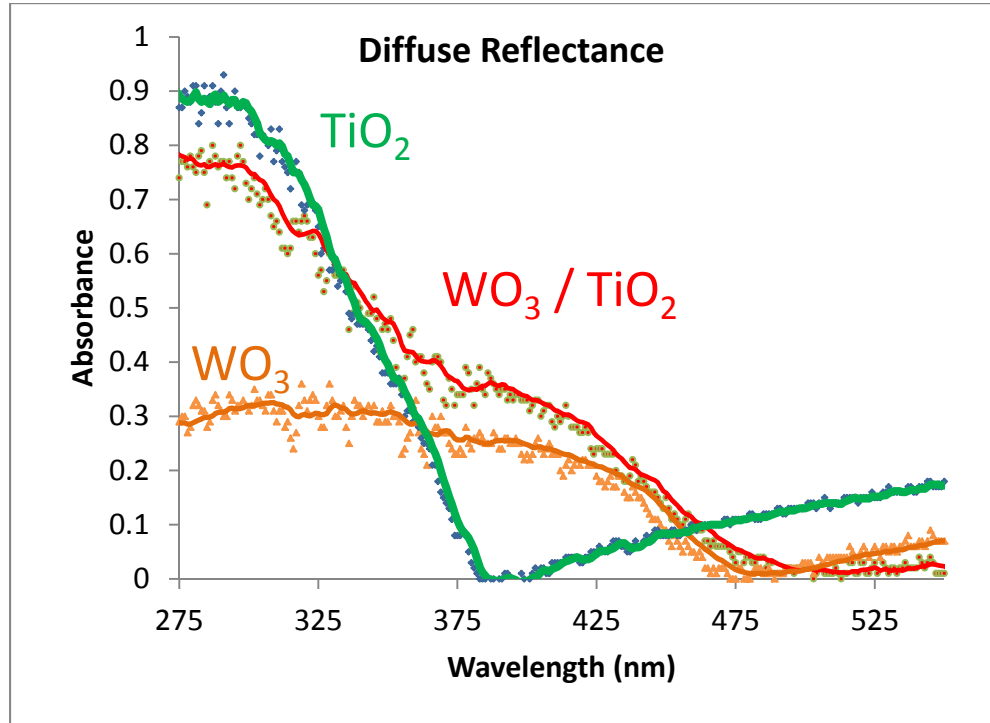
Figure 7. Absorption spectra of WO_3 (orange curve), TiO_2 nanotubes (green curve) and WO_3/TiO_2 materials (green curve).

Diffuse reflectance spectra showed in Yang's work demonstrated that WO_3 materials with no defined morphology absorbed only 30% of the UV light, agreeing with our diffuse reflectance data for pure WO_3 [26]. Optimizing the texture and thickness (~2.8 µm) of WO_3 materials, the UV absorption was 50%, keeping the same absorption onset. The authors attributed this 20% improvement to light scattering within the textured film. Our WO_3/TiO_2 composite materials absorbed almost 80% of the incident UV light, which is equivalent to a 50% increment relative to non-textured WO_3 materials, but keeping the same absorption onset on the visible region ($\Lambda \approx$ 500 nm). We attribute this absorption improvement in part to the longer absorption pathways of these nanostructures.

3.4   Morphology

The morphology of the photoelectrodes plays an important role in their performance. In particular, several studies demonstrated that organized nanostructures could improve the minority-carrier transport and reduce electron/hole recombination.   In this section, we will discuss how the synthetic parameters change the morphology of WO_3. Figure 8 shows that the WO_3 electrodeposition on a flat Ti foil, which produced a compact layer with some visible cracks.
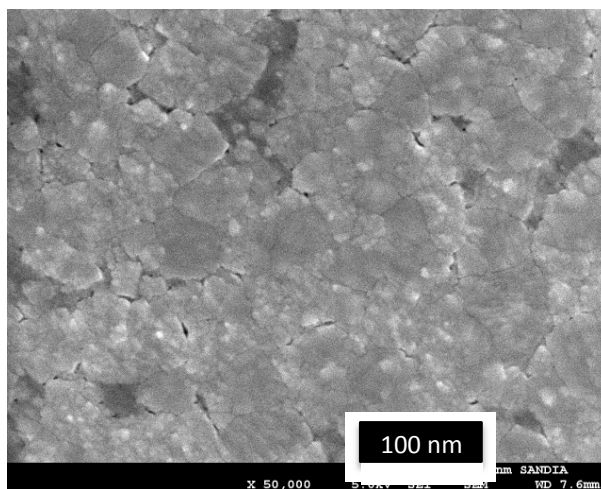
Figure 8. SEM image of WO_3 electrodeposited on Ti foil**.**

Contrary to flat substrates, the nanotubes serve as a skeleton to create thick nanostructured WO_3 materials with long absorption pathways. SEM images (Figure 9) show different nanostructures as function of WO_3 electrodeposition time.
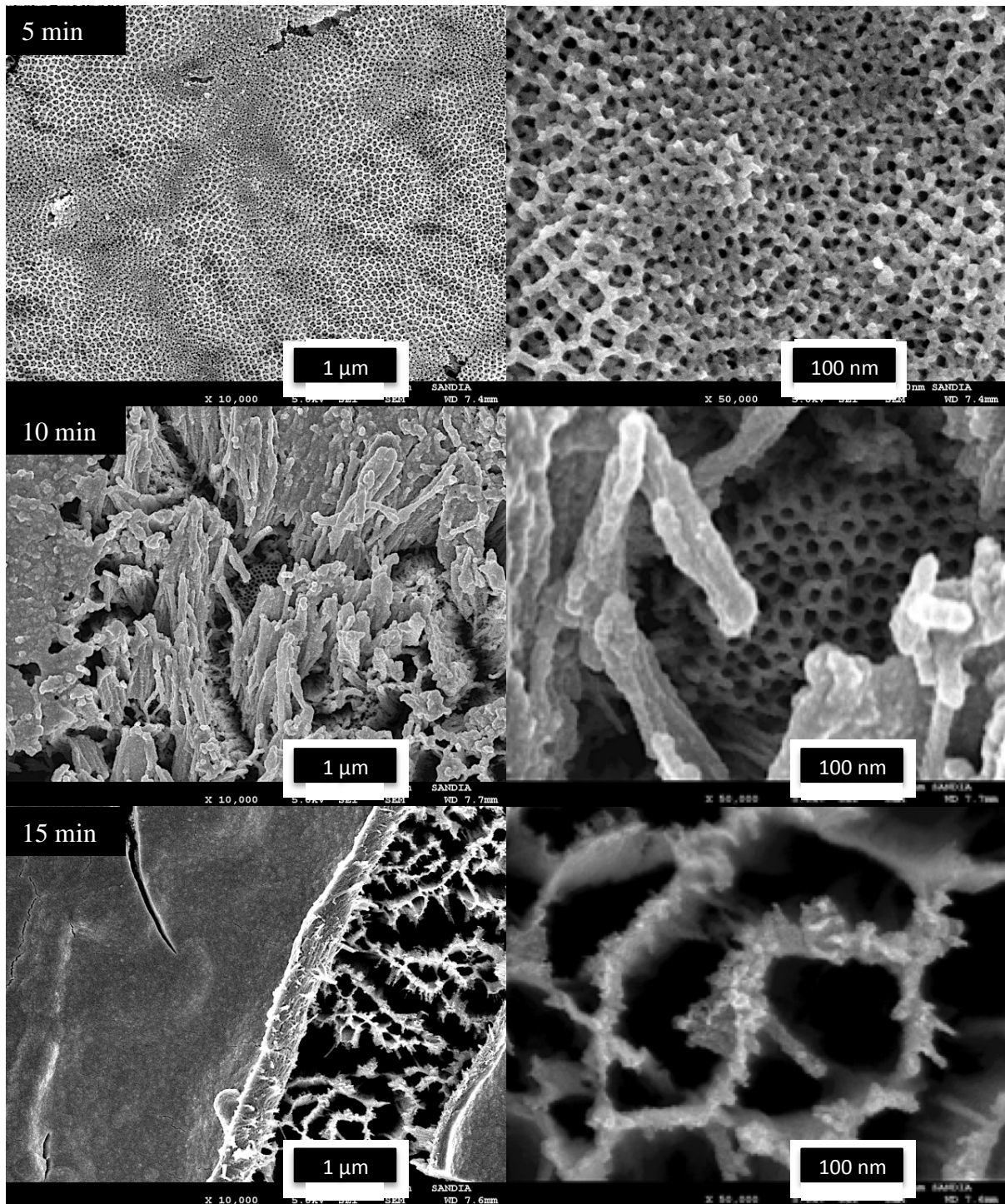
Figure 9. SEM images of WO₃/TiO₂ materials as a function of electrodeposition time.

At the beginning of the electrodeposition process, the WO_3 particles were deposited around the TiO_2 nanotube walls. After 10 min of reaction, WO_3 tubular nanostructures grew on top of the TiO_2 nanotubes. After 15 min, a cracked compact WO_3 layer was developed, covering the WO_3 nanostructures and TiO_2 nanotubes. Figure 10 shows the edge of the WO_3/TiO_2 (15 min). It has

a multilayer structure, where the bottom is the TiO_2 nanotubes on Ti foil, in the middle is WO_3 tubular nanostructures, and on the top is the WO_3 compact layer. SEM images thus demonstrate that these composite WO_3/TiO_2 materials have the same ordered structure as TiO_2 nanotubes with an external WO_3 layer, and that TiO_2 nanotubes act a skeleton to create defined nanostructures
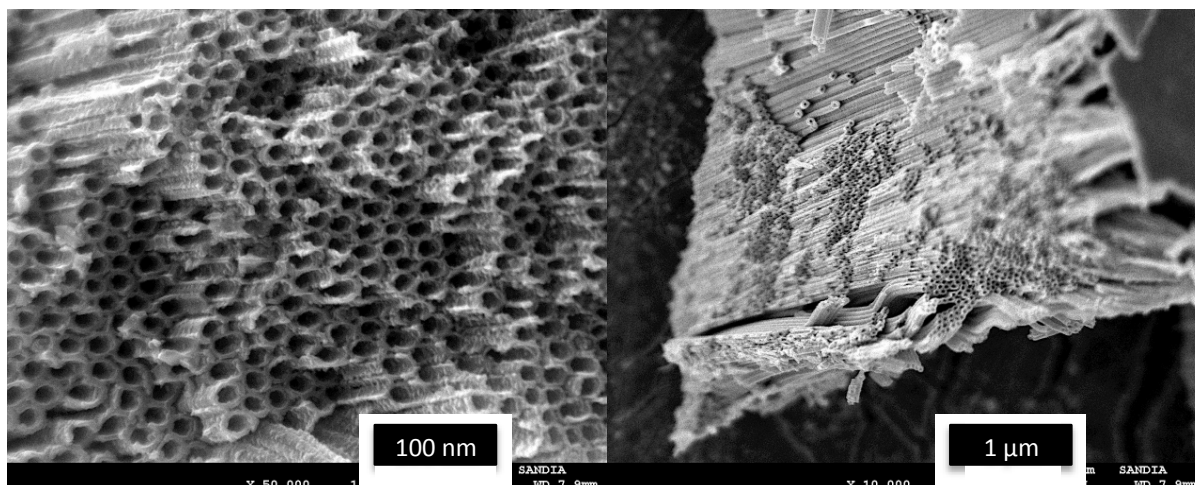
Figure 10. SEM images of the edge of WO_3/TiO_2 materials.

3.5 Effect of the morphology in the solar photo-response

Photo-electrochemical performance of these composite materials has been investigated by employing them as photoanodes in photoelectrochemical cell. For comparison purposes, WO_3, TiO_2 nanotubes and TiO_2 nanoparticles (P25) were also tested under the same conditions. The performance of WO_3/TiO_2 materials with different morphology was evaluated under visible light. Pure TiO_2 has very little visible induced photocurrent. WO_3/TiO_2 materials with low WO_3 concentration (5 min electrodeposition time) show similar response as pure WO_3. As the electrodeposition time increases, the visible induced current also increases, until a sudden decrement at higher concentration. As shown previously in Figure 9, the morphology of the materials changes with the electrodeposition time. The WO_3 tubular nanostructures prepared at 10 min electrodeposition time obtained higher photocurrent densities. The reduction in photocurrent at higher concentration is probably due to the compact layer created on the top, which could act as recombination centers, or limit the effective electrode area. The photogenerated e^-/h^+ pair would probably recombine in this compact layer before they can reach the organized nanostructures.
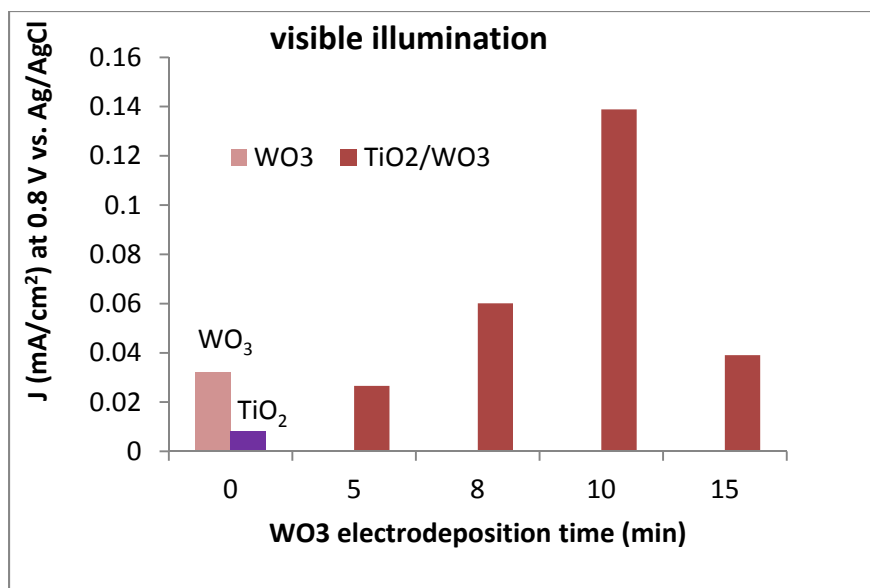
Figure 11. Photocurrent density under visible light ($\lambda > 400$ nm) as function of WO_3 electrodeposition time. Photocurrent density of bare WO_3 and TiO_2 NT were included for comparison purposes. A constant voltage of 0.8 V vs. Ag/AgCl was applied.

3.6   Incident photon to current efficiency

An important measurement is the IPCE, which determinates the ratio of the incident photons that are successfully converted in photocurrent as a function of wavelength. According to Equation 1, the IPCE depends on three processes: absorption, transport and transfer. If we compare the same bulk material, keeping constant everything except the morphology, then we can obtain information about how morphology affects the transport process. Figure 12 shows the incident photon to current efficiency (IPCE) at 0.8V vs Ag/AgCl as a function of wavelength with no co-catalyst or sacrificial reagent added the electrolyte. TiO_2 nanotubes and TiO_2 nanoparticles (P25) have the same onset, which is primarily determined by the bandgap, but the nanotubes showed a faster rise in the efficiency at decreasing wavelength. As the bandgap and the interface are the same for both electrodes, this improvement can be attributed primarily to the enhanced charge carrier transport due to the organized one-dimensional nanostructures. A WO_3 film obtained ~30% efficiency in the UV region, while TiO_2 obtained more than 50% efficiency. The efficiency onset for WO_3 and TiO_2 electrodes was 550 nm and 400 nm, respectively.

In the case of the composite WO_3/TiO_2 nanotubes, the IPCE response has the same onset as WO_3 materials, but a fast rise in the efficiency toward the UV region similar to TiO_2 nanotubes. Comparing WO_3/TiO_2 nanotubes with the individual materials, Figure 12 shows that the coupling TiO_2 with WO_3, a semiconductor with narrower bandgap, produces a red-shift in the IPCE response. Also, WO_3/TiO_2 nanotubes have a higher UV response compared to WO_3 materials. This is improvement could be attributed in part to better absorption and better transport due to the organized nanostructures. In addition, the electron transfer from TiO_2 to WO_3 results in a wide electron-hole separation, which could improve the IPCE values as well

23

[18]. Composite WO_3 and TiO_2 materials have shown a favorable electron injection from the conduction band of TiO_2 to that of WO_3 and hole transfer between valence bands in the opposite direction, which reduces e^-/h^+ recombination in both semiconductors [27].
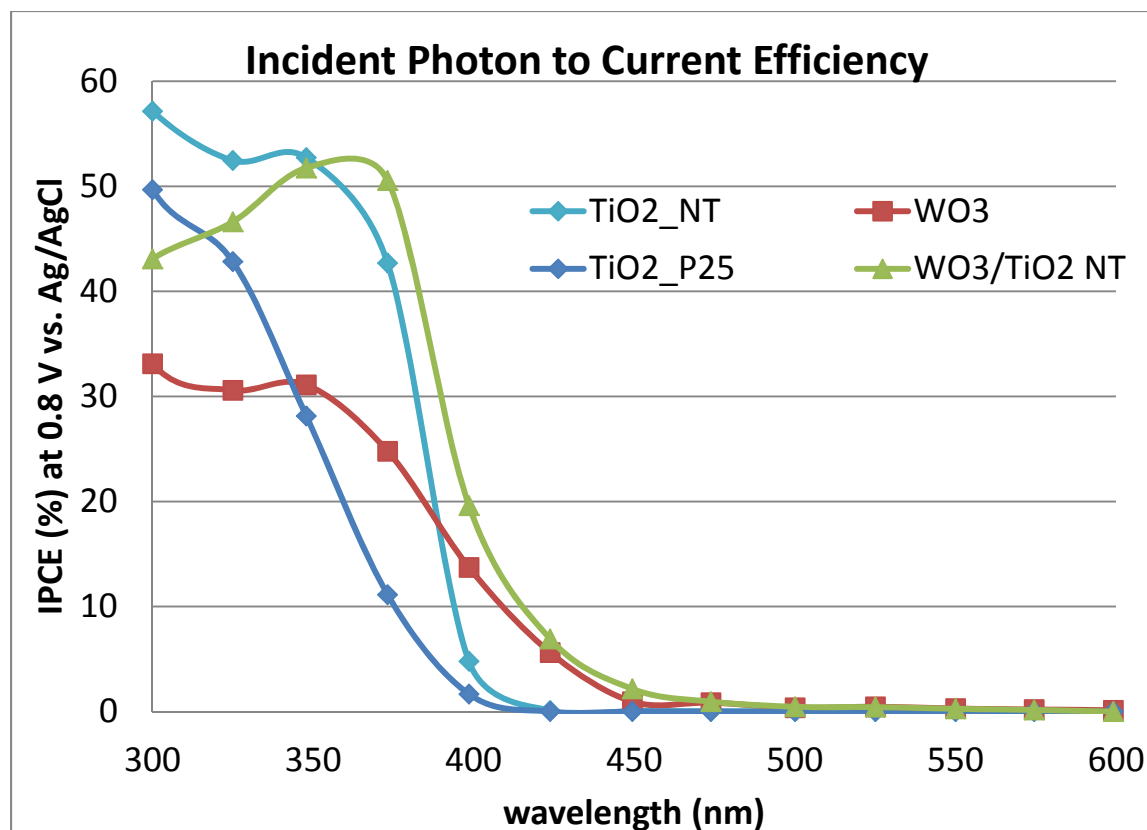
Figure 12. IPCE as function of wavelength of WO_3 (red curve), TiO_2 nanotubes (light blue curve), TiO_2 nanoparticles (blue) and WO_3/TiO_2 (green curve) electrodes. A constant voltage of 0.8 V vs. Ag/AgCl was applied.

3.7 Photoelectrochemical properties of TiO_2 and WO_3/TiO_2 nanotubes

The photoelectrochemical behavior of TiO_2 and WO_3/TiO_2 nanotubes electrodes was determined from current-potential curves obtained in 0.1 M H_2SO_4 and 0.1 M H_2SO_4 + 1 M CH_3OH solutions. Figure 13 and Figure 14 shows the photocurrent densities as a function of applied potential. The incident light from a solar simulator was chopped during the potential scan. As can be seen in both figures, the photo-responses are very fast and the dark currents are insignificant. The shape of the curves is typical of n-type semiconductor behavior. For Figure 14, a cut-off filter was used to pass only visible light ($\lambda > 400$ nm).

3.7.1 Photoelectrochemical behavior in supporting electrolyte

As shown in Figure 13, the photocurrent onset potential of WO_3/TiO_2 electrode is more positive than those for TiO_2 electrode due to the higher flat-band potential. A saturation of photocurrent is observed at +0.3 V and +0.7 V (vs. Ag/AgCl) for TiO_2 and WO_3/TiO_2 electrodes, respectively. In the case of WO_3, reports showed that control of the film morphology represents a way of optimizing photocurrent yield [26, 28]. The authors demonstrated that the photocurrent density applying 1.6 V vs. SCE can be enhanced from 0.5 to 2.2 mA/cm^2 changing the texture of the material [26]. In order to compare with our composite materials, at 0.8 vs Ag/AgCl (0.753 V vs SCE) the best film reported in Yang's work obtained equivalent to 0.54 mA/cm^2 under AM 1.5 and our WO_3/TiO_2 materials showed 0.70 mA/cm^2. Yang *et. al.* attributed the photocurrent improvement to the morphology rather than bandgap shift or doping effect.

3.7.2 Photoelectrochemical behavior in the presence of methanol

Sacrificial reagents have been used to react fast and irreversibly with the photo-generated holes resulting in higher quantum efficiency. The electrons from this oxidation reaction can reduce protons to hydrogen molecules in a process known as nonstoichiometric water splitting (Figure 1). As proof of concept, methanol (1 M) was used as model for organic pollutants and added to the electrolyte. A WO_3/TiO_2 electrode exhibited more than 5-fold increase reaching a saturated photocurrent density as high as 3.5 mA/cm^2, while TiO_2 NT exhibited 3.5-fold increase reaching around 2.5 mA/cm^2 (Figure 13). Under visible light (Figure 14), TiO_2 nanotubes obtained very small photocurrent densities, as can be seen in the inset, less than 0.007 mA/cm^2 with no significant improvement with the addition of methanol. However, WO_3/TiO_2 electrode exhibited almost 6-fold increase reaching a saturated photocurrent density of 0.65 mA/cm^2.

It is expected that the addition of methanol induces a doubling of the photocurrent and a reduction of the current onset potential compared with water oxidation alone, as observed in prior work [29, 30]. This phenomenon can be explained by the photocurrent doubling effect where an additional electron is injected in the conduction band of the electrode during the photodecomposition of methanol. Yang et. al. reported a saturated photocurrent about three times higher after the addition of methanol to the electrolyte (equivalent to 2.5 mA/cm^2 at 0.8 vs Ag/AgCl under AM 1.5) [26]. The authors suggested that the uniquely textured film might play an important role in the anomalous increases in photocurrent. In our case, the photocurrent density for WO_3/TiO_2 and TiO_2 nanotubes electrodes increased by 5-fold and 3.5-fold, respectively, with the addition of methanol. Although further studies are required to fully understand this unusual high increase in photocurrent, this is probably due to a combination of multiple factors. In addition to the photocurrent doubling effect observed by Santato et. al., and the morphology role observed by Yang, the additional improvement could be attributed to an enhancement of the interface efficiency due to rapid and irreversible consumption of the photogenerated holes, which suppress the e$^-$/h$^+$ recombination in the interface.
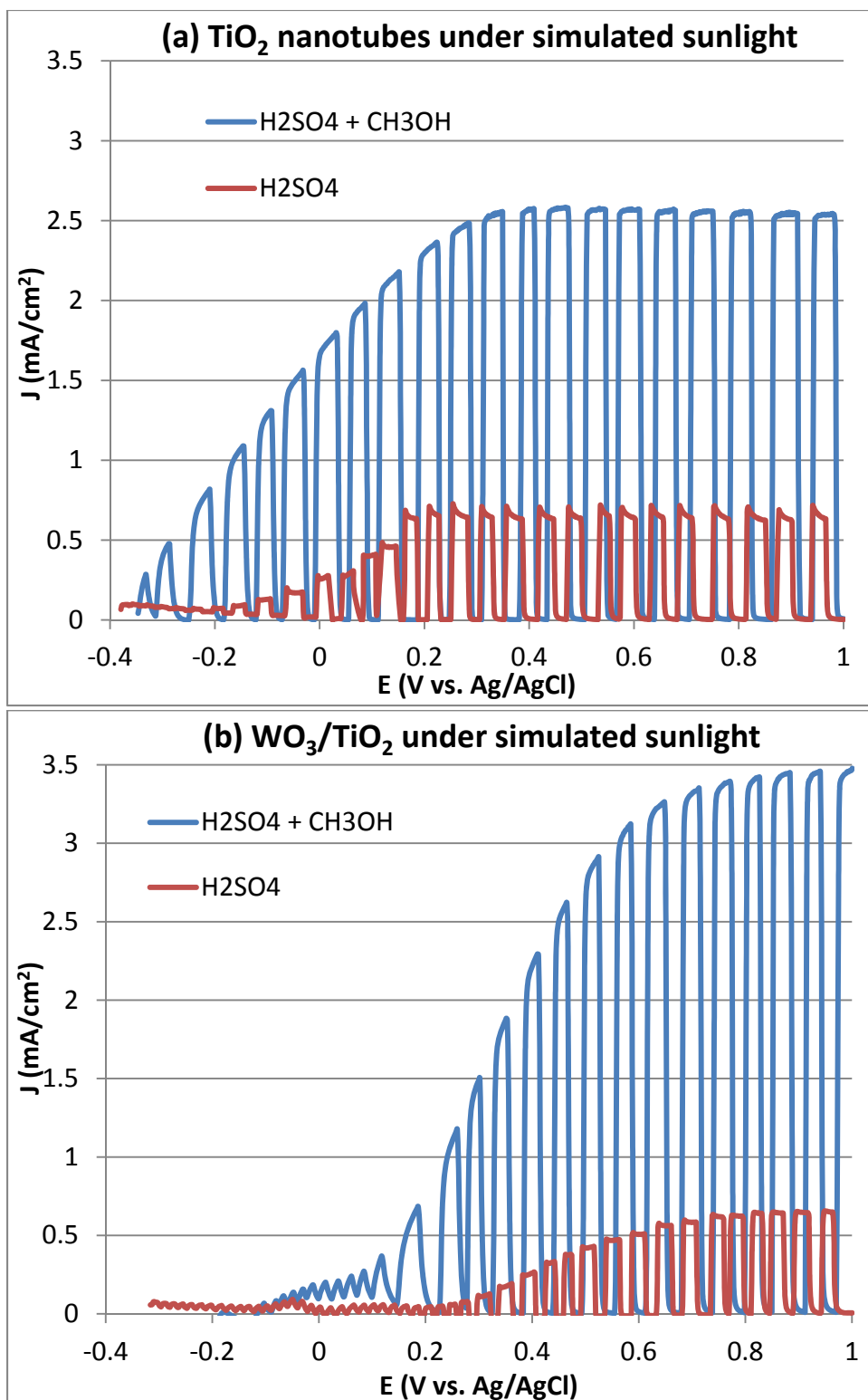
Figure 13. Photocurrent density of (a) TiO$_2$ NT and (b) WO$_3$/TiO$_2$ NT under intermittent simulated sunlight using 0.1M H$_2$SO$_4$ as electrolyte (red curve) and adding 1M methanol (blue curve).
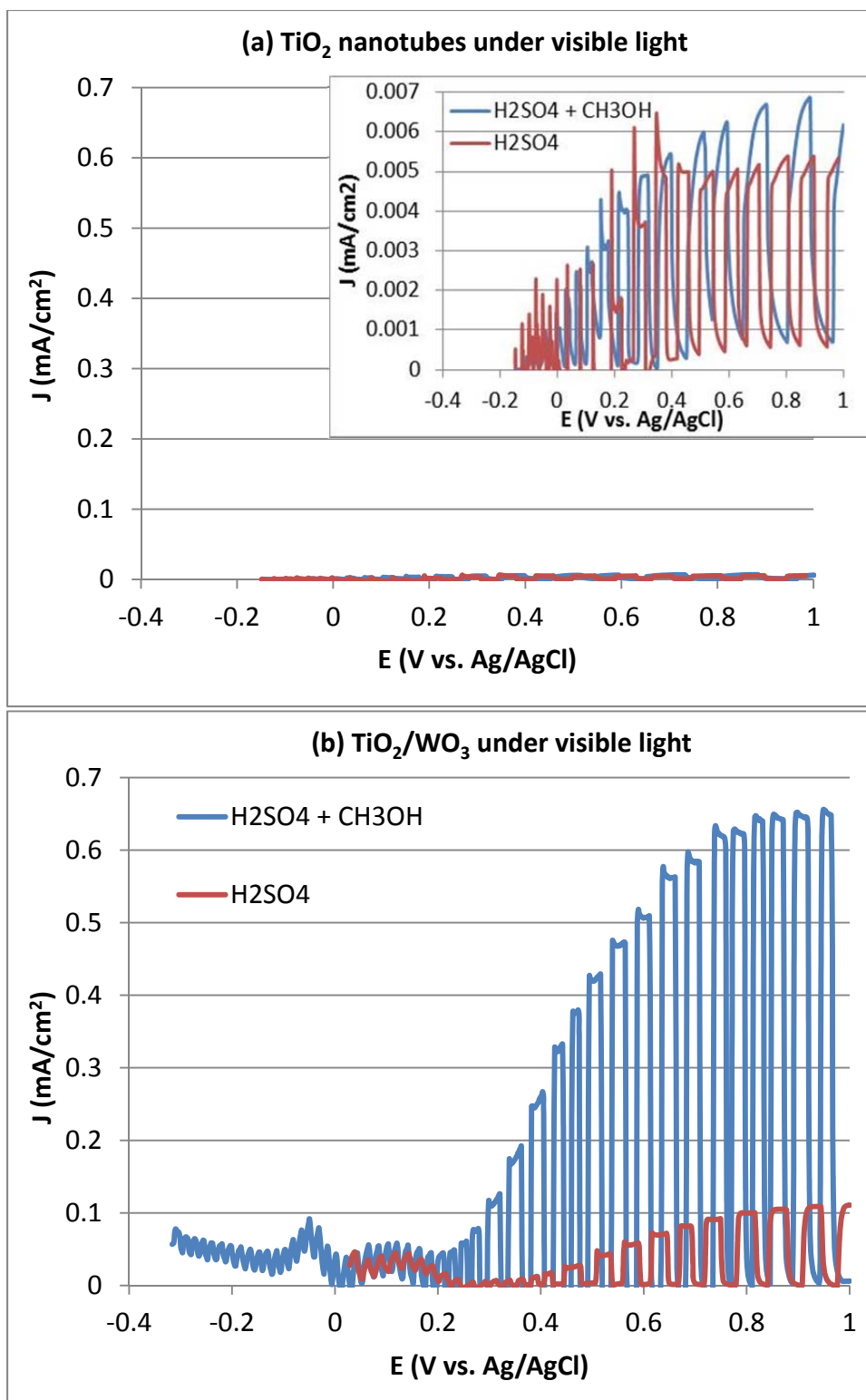
Figure 14. Photocurrent density of (a) TiO_2 NT and (b) WO_3/TiO_2 NT under intermittent visible light ($\lambda < 400$ nm) using 0.1M H_2SO_4 as electrolyte (red curve) and adding 1M methanol (blue curve).

An additional improvement in the photocurrent with the addition of methanol was observed for the composite materials relative to TiO_2 nanotubes (approximately 1 mA/cm^2 higher photocurrent densities). As shown in Figure 14, the photoresponse under visible light increased by more than 6-fold for the composite material, however, the TiO_2 nanotubes didn't show a significant improvement. A moderate improvement in the visible absorption and IPCE values in $\lambda > 400$ nm can make a significant increment in the solar photocurrent density taking a consideration that 44 % of the sunlight is visible and only 3 % UV.

3.8   Simultaneous photodegradation of organic pollutants

Photocatalytic decomposition of organic pollutants and production of clean hydrogen fuel can take place simultaneously when the pollutants are acted as electron donors [31, 32]. Li et. al. reported enhanced photocatalytic hydrogen production using aqueous Pt/TiO_2 suspension in the presence of pollutants (oxalic acid, formic acid and formaldehyde) acting as electron donors [17]. Despite the limited work on using pollutants as electron donors, the encouraging results show the promise of the integration of pollutant decomposition and clean hydrogen production.

3.8.1 Photocurrent density as a function of organic pollutant concentration

In addition to methanol, we studied formic acid and formaldehyde, two common organic pollutants found in wood and leather industrial wastewater and ethylene glycol, a deicing agent found in airport and road drainage. Figure 15 shows the photocurrent density as function of the concentration of different organic compounds (pollutants). In all the cases, increasing the concentration of the pollutants resulted in an increase of the photocurrent densities. WO_3/TiO_2 electrodes produced higher photocurrent densities compared to bare TiO_2 electrodes. For WO_3/TiO_2 electrode, the photocurrent density exhibited a 5.3-fold increase with formaldehyde, 4.6-fold increase with formic acid and 4.4-fold increase with ethylene glycol. For the TiO_2 electrode, the photocurrent density exhibited a 4-fold increase formic acid, 3.6-fold increase formaldehyde, and 3-fold increase with ethylene glycol.
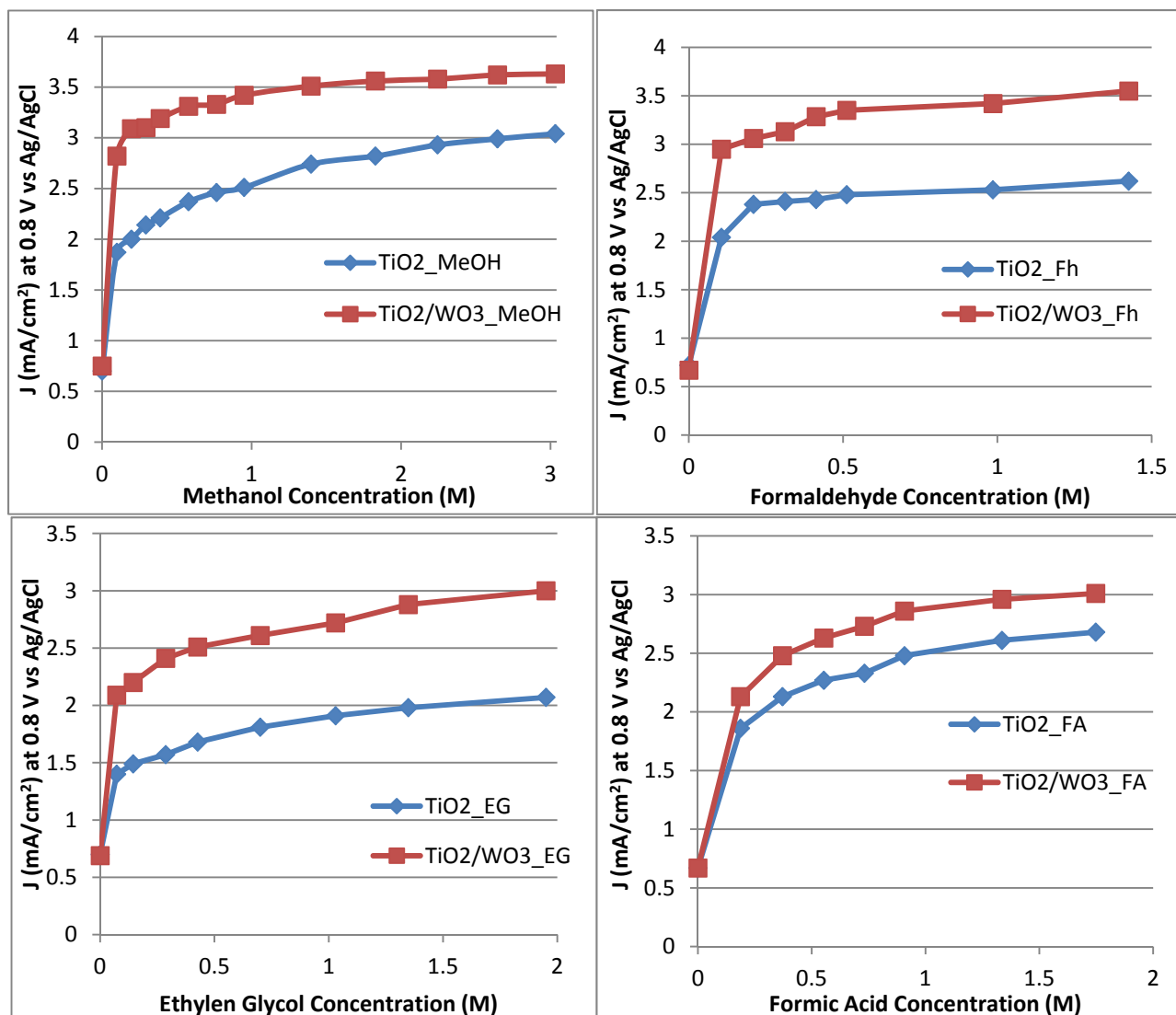
Figure 15. Photocurrent density as function of different organic compounds concentration. All experiments were carried out under constant voltage of 0.8 V vs. Ag/AgCl.

3.8.2 *Chemical oxygen demand measurements*

Chemical Oxygen Demand (COD) is used to indirectly measure the amount of organic compounds in surface water and wastewater. In this work, COD measurements were used to follow the degradation progress of methanol and formaldehyde during the photoreaction. A 0.5 cm^2 electrode was illuminated using a sunlight simulator. The quartz cell was covered with parafilm to avoid evaporation and aliquots were taken at different times. A control experiment (blank) was performed under the same conditions, except with no electrodes, to determine spontaneous photodegradation. Figure 16 shows COD removal efficiency, calculated according Equation 3, as a function of illumination time. The COD initial value was 5000 ppm and 3000 ppm for methanol and formaldehyde, respectively. The blank experiment for methanol showed ~ 5 % loss for evaporation, while for formaldehyde the loss was negligible. For TiO_2 electrode,

the COD removal efficiency quickly increased to 15 % in the first half hour of illumination. For the next 4.5 h, the efficiency slowly increased up to 20 %. In the case of WO_3/TiO_2 electrode, the COD removal efficiency reached 17 % in the first half hour and 35 % after 5 h. The COD formaldehyde removal efficiency shows a more linear increment rate reaching 34 % and 42 % for TiO_2 and WO_3/TiO_2 electrode, respectively.
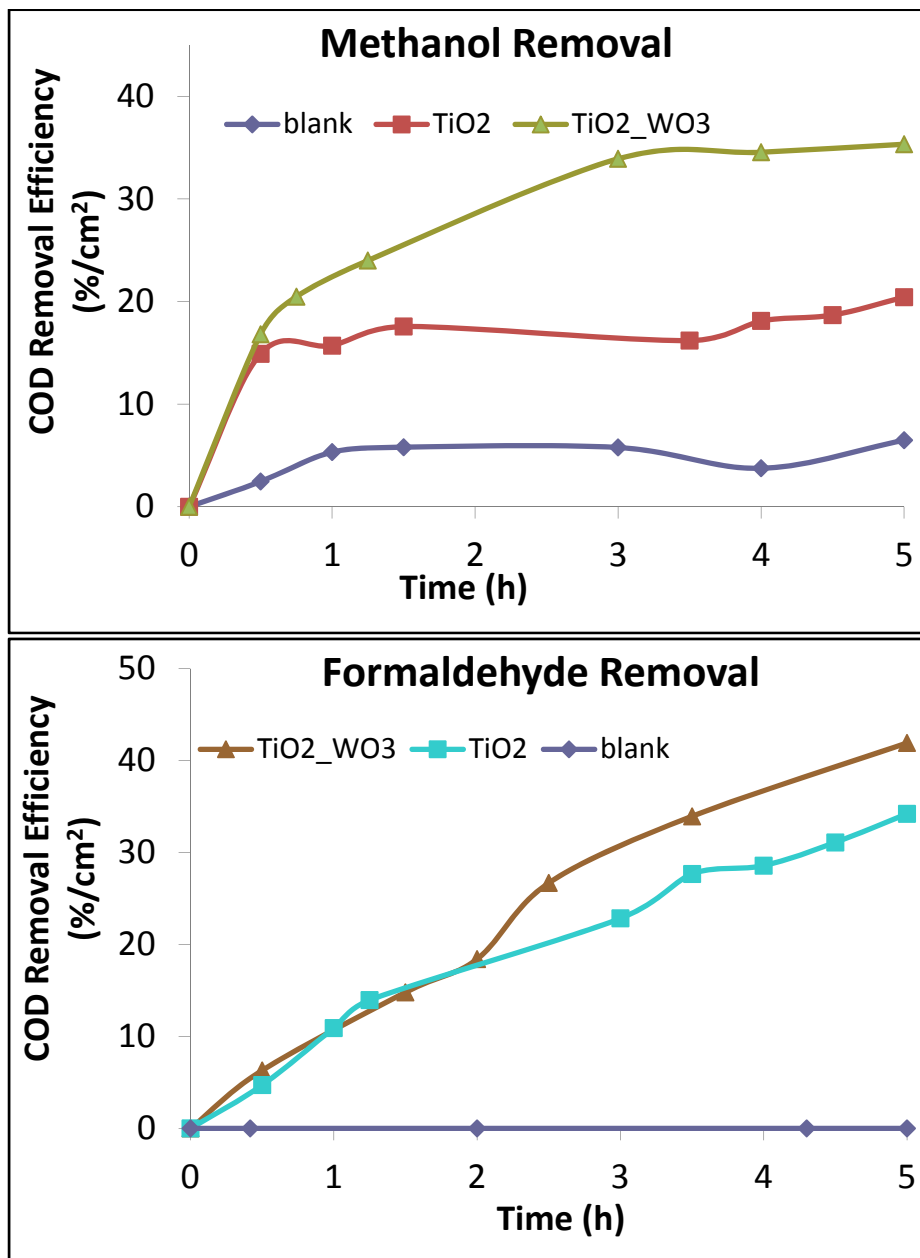

Figure 16. COD removal efficiency of methanol and formaldehyde. The experiment was carried out under constant voltage of 0.8 V vs. Ag/AgCl.

4. Conclusions

In this work, we demonstrated a low-cost synthetic approach to create WO_3/TiO_2 nanostructures. These materials were employed as photoanodes in a photoelectrochemical cell for the degradation of organic pollutants and the simultaneous generation of photocurrent for hydrogen production. We demonstrated that each process in the operation of the photoelectrochemical cell can be improved without jeopardizing the other processes, which resulted in an overall efficiency improvement. Contrary to other bandgap reduction techniques, we showed that composite WO_3/TiO_2 nanostructures improved the solar spectrum absorption as well as the charge carrier transport. WO_3/TiO_2 electrodes were more active that TiO_2 or WO_3 alone for optical and photoelectrochemical measurements. Diffuse reflectance spectra show an improvement in the visible absorption relative to bare TiO_2 nanotubes and in the UV absorption relative to bare WO_3 films. Comparing the absorption spectrum and IPCE plot, we can conclude that for all the wavelengths that the composite electrodes absorb photons, a photocurrent is generated. These composite nanostructures showed an improvement in the photogenerated carrier transport and the absorption pathways, resulting in higher IPCE efficiencies. In addition, the electrode/electrolyte interfacial transfer was improved by incorporating the fast and irreversible oxidation of organic pollutants, resulting in higher photocurrents that can be used to drive reduction reactions. These WO_3/TiO_2 nanostructured and related materials are interesting candidates to drive simultaneous photochemical reactions, such as water reduction (H_2 production) and oxidation of pollutants.

5. Future work

In this work, we developed unique nanostructured photoanodes with enhanced optical and photoelectrochemical properties to perform oxidation reactions. We proved that in the presence of common organic pollutants the photocurrent densities are significantly higher. These enhanced photocurrent densities drive reduction reactions at the cathode, allowing the useful production of hydrogen.

Because the conduction band of WO_3 is not negative enough for water reduction, some modifications are needed to achieve H_2 evolution. The application of external voltage, the use of pH gradients, and hybrid devices consisting of photoelectrochemical and photovoltaics components are popular alternatives [33]. In addition, band gap engineering techniques can be used to modify the valence band of WO_3 using different elements and co-catalysts. A very promising alternative is coupling n-type WO_3 with p-type photocatalyst for water reduction half-reaction (H_2 production). For instance, photocatalytic water splitting into H_2 and O_2 under visible-light irradiation was demonstrated using the oxynitride Pt–TaON for H_2 evolution and a Pt–WO_3 catalyst for O_2 evolution in an IO_3^-/I^- shuttle redox-mediated system [34]. Another proposed couple to produce clean H_2 without wires (applied voltage) is n-type WO_3 and p-type Si [8].

Definitely more work is needed to achieve a commercial photoelectrochemical cell for simultaneous wastewater treatment and H_2 production. However, this work shows that WO_3/TiO_2 nanostructures are very promising candidates to drive these photo-conversion reactions in an efficient way.

6. References

1. Shankar, K., et al., *Recent Advances in the Use of TiO2 Nanotube and Nanowire Arrays for Oxidative Photoelectrochemistry.* Journal of Physical Chemistry C, 2009. **113**(16): p. 6327-6359.
2. Ilieva, M., A. Nakova, and V. Tsakova, *TiO2/WO3 hybrid structures produced through a sacrificial polymer layer technique for pollutant photoand photoelectrooxidation under ultraviolet and visible light illumination.* J Appl Electrochem, 2012. **42**: p. 121-129.
3. Shankar, K., et al., J. Phys. Chem. C, 2009. **113**: p. 6327-6359.
4. Kamat, P.V., J. Phys. Chem. C, 2007. **111**: p. 2834-2860.
5. Boettcher, S.W., et al., *Energy-Conversion Properties of Vapor-Liquid-Solid-Grown Silicon Wire-Array Photocathodes* Science, 2010. **327**: p. 185-187.
6. Spurgeon, J.M., et al., *Repeated Epitaxial Growth and Transfer of Arrays of Patterned, Vertically Aligned, Crystalline Si Wires from a Single Si(111) Substrate.* Appl. Phys. Lett., 2008. **93**: p. 032112.
7. Kayes, B.M., et al., *Synthesis and Characterization of Silicon Nanorod Arrays for Solar Cell Applications.* Proc. IEEE, 2006: p. 221.
8. Reyes-Gil, K.R., J.M. Spurgeon, and N.S. Lewis, *Silicon and Tungsten Oxide Nanostructure for Water Splitting.* Proc. SPIE, 2009. **7408**: p. 740826.
9. Mor, G.K., et al., *Use of highly-ordered TiO2 nanotube arrays in dye-sensitized solar cells.* Nano Lett., 2006. **6**: p. 215-218.
10. Beranek, R., et al., *Enhancement and limits of the photoelectrochemical response from anodic TiO2 nanotubes.* App Phys. Lett., 2005. **87**: p. 243114
11. Kongkanand, A., R.M. Dominguez, and P.V. Kamat, *Single Wall Carbon Nanotube Scaffolds for Photoelectrochemical Solar Cells. Capture and Transport of Photogenerated Electrons.* Nano Lett., 2007. **7**: p. 676.
12. Benoit, A., et al., *Decoration of TiO2 nanotube layers with WO3 nanocrystals for high-electrochromic activity.* Electrochemistry Communications, 2009. **11**(4): p. 728-732.
13. Nah, Y.-C., et al., *TiO2−WO3 Composite Nanotubes by Alloy Anodization: Growth and Enhanced Electrochromic Properties.* Journal of the American Chemical Society, 2008. **130**(48): p. 16154-16155.
14. Nah, Y.-C., et al., *Enhanced electrochromic properties of self-organized nanoporous WO3.* Electrochemistry Communications, 2008. **10**(11): p. 1777-1780.
15. Paulose, M., et al., *Anodic growth of highly ordered TiO2 nanotube arrays to 134 microm in length.* J. Phys. Chem. B, 2006. **110**: p. 16179.
16. Shankar, K., et al., *Highly-ordered TiO2 nanotube arrays up to 220 μm in length: use in water photoelectrolysis and dye-sensitized solar cells.* Nanotechnology, 2007. **18**.
17. Li, Y., G. Lu, and S. Li, *Photocatalytic production of hydrogen in single component and mixture systems of electron donors and monitoring adsorption of donors by in situ infrared spectroscopy.* Chemosphere, 2003. **52**: p. 843-850.
18. Roy, P., S. Berger, and P. Schmuki, *TiO2 Nanotubes: Synthesis and Applications.* Angew. Chem. Int. Ed., 2011. **50**: p. 2904-2939.

19. Yang, M., N.K. Shrestha, and P. Schmuki, *Thick porous tungsten trioxide films by anodization of tungsten in fluoride containing phosphoric acid electrolyte* Electrochem. Commun., 2009. **11**: p. 1908-1911.

20. Lai, C.W., S. Sreekantan, and P. San E, *Effect of radio frequency sputtering power on W–TiO2 nanotubes to improve photoelectrochemical performance.* Journal of Materials Research, 2012. **27**(13): p. 1695-1704.

21. Pauporté, T., *A Simplified Method for WO[sub 3] Electrodeposition.* Journal of The Electrochemical Society, 2002. **149**(11): p. C539.

22. Howard, C.J., V. Luca, and K.S. Knight, *High-temperature phase transitions in tungsten trioxide—the last word?* J. Phys.: Condens. Matter, 2002. **14**: p. 377.

23. Xin, G., W. Guo, and T. Ma, *Effect of annealing temperature on the photocatalytic activity of WO3 for O2 evolution.* Applied Surface Science, 2009. **256**: p. 165.

24. Hong, S.J., H. Jun, and J.S. Lee, *Nanocrystalline WO3 film with high photo-electrochemical activity prepared by polymer-assited direct deposition.* Scripta Materialia, 2010. **63**: p. 757.

25. Bamwenda, G.R. and H. Arakawa, *The visible light induced photocatalytic activity of tungsten trioxide powders.* Appl. Catal. A, 2001. **210**: p. 181.

26. Yang, B., et al., *Tungsten Trioxide Films with Controlled Morphology and Strong Photocatalytic Activity via a Simple Sol-gel Route* Catal. Lett., 2007. **118**: p. 280-284.

27. Georgieva, J., et al., *Enhanced photocatalytic activity of electrosynthesised tungsten trioxide–titanium dioxide bi-layer coatings under ultraviolet and visible light illumination.* Electrochemistry Communications, 2007. **9**: p. 365-370.

28. Yang, B., et al., *Enhanced Photoelectrochemical Activity of Sol-Gel Tungsten Trioxide Films through Textural Control.* Chemistry of Materials, 2007. **19**(23): p. 5664-5672.

29. Santato, C., et al., *Crystallographically Oriented Mesoporous WO₃ Films: Synthesis, Characterization, and Applications.* J. Am. Chem. Soc., 2001. **123**: p. 10639-10649.

30. Wahl, A. and J. Augustynski, *Photoelectrochemical analysis of anion-doped TiO2 colloidal and powder thin-film electrodes.* J. Phys. Chem. B, 1998. **102**: p. 7820.

31. Ostachaviciute, S., J. Baltrusaitis, and E. Valatka, *Photoactive WO3 and Se-WO3 thin films for photoelectrochemical oxidation of organic compounds.* Journal of Applied Electrochemistry, 2010. **40**(7): p. 1337-1347.

32. Habazaki, H., Y. Hayashi, and H. Konno, *Characterization of electrodeposited WO3 films and its application to electrochemical wastewater treatment.* Electrochimica Acta, 2002. **47**(26): p. 4181-4188.

33. Esposito, D.V., et al., *Hydrogen production from photo-driven electrolysis of biomass-derived oxygenates: A case study on methanol using Pt-modified WO3 thin film electrodes.* International Journal of Hydrogen Energy, 2011. **36**(16): p. 9632-9644.

34. Abe, R., et al., *Photocatalytic overall water splitting under visible light by TaON and WO3 with an IO3 2/I2 shuttle redox mediator.* Chem. Commun., 2005: p. 3829–3831.

Distribution

4 Lawrence Livermore National Laboratory
   Attn: N. Dunipace
   P.O. Box 808, MS L-795
   Livermore, CA 94551-0808

1 MS0899 Technical Library 9536 (electronic copy)

1 MS9403 Karla Reyes 8223

1 MS9291 David B. Robinson 8651